ELSEVIER

Ultramicroscopy 81 (2000) 289–300

ultramicroscopy

www.elsevier.nl/locate/ultramic

Electron microscope characterization of CdSe/ZnSe quantum dots based on molecular dynamics structure relaxations

K. Scheerschmidt[a,*], D. Conrad[a], H. Kirmse[b], R. Schneider[b], W. Neumann[b]

[a]*Max Planck Institute of Microstructure Physics, Weinberg 2, D-06120 Halle, Germany*
[b]*Institute of Physics, Humboldt University of Berlin, Invalidenstr. 110, D-10115 Berlin, Germany*

Received 25 June 1999; received in revised form 5 October 1999

Dedicated to Professor Harald Rose on the occasion of his 65th birthday

Abstract

Molecular dynamics simulations using empirical potentials are applied to characterize the structure, the energy relaxation and the stability of pyramidal-shaped quantum dots in the CdSe/ZnSe system. The relaxed structure models are used for a reliable interpretation of electron microscope investigations to analyze the size, the shape and the strain fields of the quantum dots. Though the elastic strains modify the electron microsope image contrast by creating virtual truncations of the pyramids or additional black–white lobes, optimum imaging conditions chosen will reveal the shape and the size of the dots.

PACS: 02.70.Ns; 34.20; 61.16; 61.34

Keywords: Quantum dots; Molecular dynamics; Electron microscope structure characterization

1. Introduction

Quantum dots (QD) and other structural modifications with reduced dimensions in semiconductors are of interest in microelectronics because of their significant optical and electronic properties due to the quantum confinement of the electron wave function (see, e.g., the reviews [1,2]). Two main problems are of particular interest: the control of the self-assembled growth of QDs, and the dependence of the opto-electronic properties on the QD structure, i.e., the influence of the shape, the size and the strain due to the misfit between the lattices of the dot and the matrix. To solve the problems QDs are frequently investigated by atomic force microscopy, scanning tunneling microscopy, spectroscopic methods, etc. In addition, conventional transmission electron microscopy (TEM) – mostly as plan-view imaging – and cross-sectional high-resolution electron microscopy (HREM) have been applied to investigate the QD structure at an atomic level. For capped quantum dots electron microscope imaging is the only direct method of structure investigation without destroying the buried QDs.

The size and the shape of molecular beam epitaxy (MBE) grown QDs depend strongly on the

* Corresponding author. Tel.: + 49-345-5582910; fax: + 49-345-5582917.
E-mail address: schee@mpi-halle.de (K. Scheerschmidt)

0304-3991/00/$ - see front matter
PII: S0304-3991(99)00185-0

growth mode. This can directly be investigated, e.g., by studying the moiré fringes in plan-view TEM images during the QD growth [3]. Thus a great variety of dot shapes have been proposed and theoretically investigated as, e.g., lens-shaped dots, conical islands, and pyramids with different side facets of types $\{0\,1\,1\}$, $\{1\,1\,1\}$, $\{1\,1\,2\}$, $\{1\,1\,3\}$, and $\{1\,3\,6\}$. Band structure calculations for strained dots based on the elasticity theory or using structure relaxations with simple valence force fields have demonstrated that the wave function and energies are very sensitive to the underlying strain distribution [4]. Similarly, a strong modification of the electron microscope image contrast has been revealed by the strain field calculations using molecular static energy minimization based on many-body cluster potentials [5]. Here, the main differences in the image contrast between the relaxed and the unrelaxed pyramids are the virtual truncation and the black–white lobes around the top of the pyramids in the cross-sectional HREM images. The investigated InAs islands of pyramidal shape always seem to be truncated owing to a lower In content on top of the pyramid and to the high level of strain around the island. For technical reasons, in [5] it was impossible to calculate the plan-view images, too. But the diffraction contrast was simulated for the cross-sectional orientation, allowing one to discuss the depth dependency of the contrast of the pyramids and the possibilities and limitations of the size and shape analyses, bestowing great caution on interpreting the images. Not reflecting these results, in [6] the same caution is demanded. However, simulations using only spherical inclusions or displacement fields in isotropic media cannot explain the HREM images of non-spherical structures and the influence of anisotropy, respectively. Here, better results may be revealed using the diffraction contrast analysis of non-spherical inclusions [7], cubes or ellipsoids in anisotropic media [8], or applying finite element methods to evaluate the strain fields (FEM; see, e.g., [9–11]).

However, the atomic processes determine the behavior of extended defects at a microscopic level, thus influencing the macroscopic properties. While, in principle, it is now possible to predict material properties by using quantum-theoretical ab initio calculations with a minimum of free parameters, the only method of simulating atomic processes with macroscopic relevance is the molecular dynamics (MD) method using suitably fitted many-body empirical potentials. Such simulations enable a large number of particles (10^4–10^9) and sufficient relaxation times (10–1000 ps) to be considered.

In the following, MD simulations of CdSe QDs in the ZnSe matrix are discussed to gain a better understanding of the structural modifications due to relaxation and of the resulting TEM and HREM contrast modifications, both necessary for an improved image interpretation. The present work is based on the experimental investigations described in detail in [12] and the preliminary contrast interpretations using plan-view MD and TEM simulations [13].

2. Method

The method of molecular dynamics (MD) solves Newton's equations of motion for a molecular system, which results in trajectories for all particles considered in the system. Thus MD provides a tool suitable for simulating time-dependent processes at an atomic level as, e.g., the growth of crystals, the reordering of interfaces, the interaction between adatoms and surfaces as well as the relaxation of core structures of lattice defects. The calculations are performed with the fifth-order predictor-corrector algorithm of Gear [14] using a constant volume (NVE ensemble) or a constant pressure (NpT ensemble) and time steps of the order of 0.25 fs to ensure the proper calculation of all possible modes. NVE is preferred for free surfaces or simulations to calculate diffusion constants, whereas NpT enables the relaxation of the cell dimensions and the application of an outer pressure, which is important for, e.g., the reordering process at interfaces. For controlling the system temperature either all particle velocities are slightly rescaled at each time step, or solely the outer layers of the structure model, but still applying periodic boundary conditions parallel to interfaces. In the latter case, the energy dissipation is controlled by the transfer rates of the kinetic energy at the borders of the model describing an energy flux into a macroscopic

substrate. In addition, for straight defects relaxing the misfit at interfaces the system is coupled elastically to the bulk surrounding matrix.

The interatomic forces in covalent solids can sufficiently be described only if the influence of the local environment according to the electronic structure is included. Simple pair potentials and potentials of the valence force field or related types as, e.g. the Keating (K) potential, are restricted in their validity to small deviations from the equilibrium. However, empirical potentials have been developed, which allows the calculation of the many-body interaction sufficiently well. The potential most often used for semiconductors is the Stillinger–Weber (SW) potential [15], consisting of 2- and 3-body interactions, with a smooth cut-off mostly behind the nearest-neighbor distance, and which is fitted to the cohesive energy, the lattice parameter, and the elastic constants or the melting point. Though it fails for large distortions in the surrounding of defects, it allows the second next neighbor interaction to be included by rescaling. The potential of Tersoff [16] (here there are at least three parametrizations TI, TII, TIII) consists of a third-order cluster structure and is a bond-order potential, thus having a functionality other than SW.

Most of the potentials available are of the SW or T types. They offer advantages and disadvantages in the range of validity, physical meaning, fitting and accuracy as well as applicability [17]. Such restrictions exist for other potential types, too, even if the embedded atom approximation is used (EAM) or special environmental dependencies are constructed to enhance the elastic properties near defects. In addition, all potentials are not well applicable to long-range interactions, and the electronic structure and the nature of the covalent bonds can only be described indirectly. Therefore, it is of importance to find physically motivated semiempirical potentials and to use suitable methods to fit to first principle as well as experimental data bases. We have intensively tested different parametrizations of the SW and T potentials. For the present calculations we applied our own parametrization of the Stillinger–Weber potential fitted to the cohesive energy, the lattice constant, and the elastic constants, similar to that of [18] for the CdTe interaction. The parameters used (r_0, ε, A, B, and γ_2) are given in Table 1, for the functionality and the parametrization cf. the original papers [15,18]. The additional parameters $\lambda = 21.0$, $a = 1.8$, $\gamma_3 = 1.2$, and $\cos\theta_0 = -1/3$ of the fitted SW potential are the same for all interactions considered (cf. [15,18,19]). Thus the interactions Cd–Se and Zn–Se are included completely, whereas an intermixing of Cd and Zn is avoided by controlling the topology of the QDs. Therefore, the simulations of the stability of the QDs are valid as long as no direct interaction occurs between Cd and Zn during intermixing. The embedded QDs are relaxed at 0 K for at least 10 000 time steps of 0.25 fs, i.e. for 250 ps. Then annealing follows up to some 600 K so that the system is always near the equilibrium at each temperature step, i.e. holding again about 250 ps per step.

Table 1
Parametrization of the Stillinger–Weber potential for Cd–Zn–Te–Se

	r_0 (Å)	ε (eV)	A	B	γ_2
ZnSe	2.455	2.19	6.736385	0.32509	1.2351
ZnTe	2.641	1.955	8.607706	0.35070	1.3777
CdSe	2.620	1.955	6.637040	0.31986	1.2049

The atomic structures of the CdSe QDs in the ZnSe matrix are prescribed by geometric models as demonstrated in Fig. 1 by using the CERIUS [20] package. Besides this, the CERIUS package is used only for prerelaxations with simple many-body potentials or the valence force fields and creating data bases for the potential fit. The following annealing and relaxation simulations are based on an own program as described in general above. The starting configurations are supercells in $\{1\,0\,0\}$ orientation of $13 \times 13 \times 13$ unit cells with 17 576 atoms and a resulting box length of 7.31 nm. The base length of the dots is about 6 nm. In $\{1\,1\,0\}$ representation, necessary for comparing the simulations with respective HREM investigations, the structure is transformed into [1 1 0] by $1/\sqrt{2} \times \sqrt{2} \times 1$ supercell enlargement and contains 16 848 atoms. Alternatively, larger cells with the same QDs ($16 \times 16 \times 16$, box length 8.82 nm) and smaller dots within the original boxes (base length 5.3 nm) and

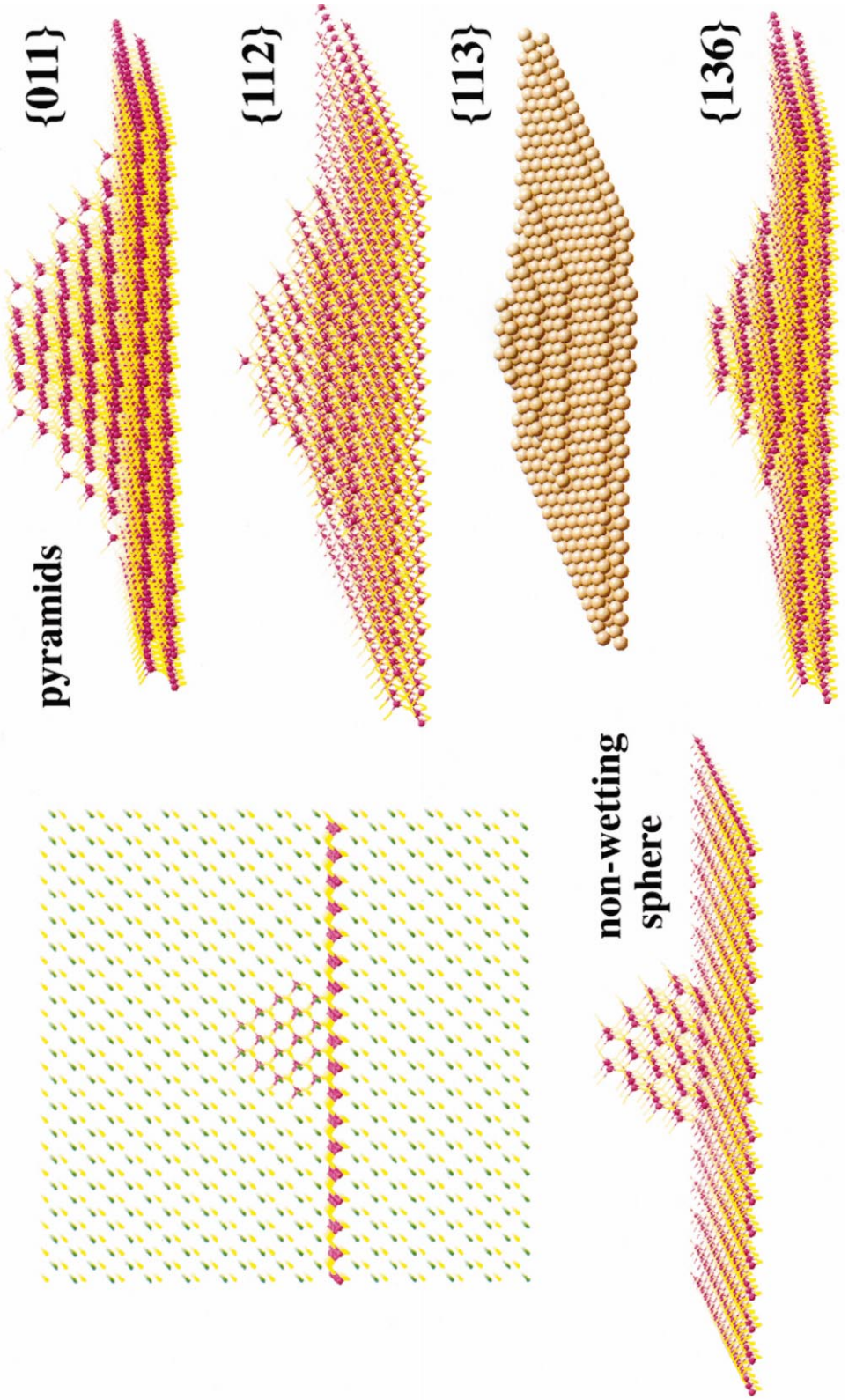
pyramids
{011}
{112}
{113}
{136}
non-wetting
sphere

the respective transformations are used to investigate the effects of the self-influence of QDs in smaller cells due to periodic boundary conditions.

Four different QDs with facets $\{0\,1\,1\}$, $\{1\,1\,2\}$, $\{1\,1\,3\}$ and $\{1\,3\,6\}$ are presented in Fig. 1. Additionally, on the left-hand side the embedding is demonstrated for a spherical QD showing the embedded dot and the isolated one. The most important difference of the various structures consists in the varying step structure of the facets due to their different inclination. Other configurations, e.g. $\{1\,1\,1\}$ facetting, and different orientations are simulated, too, as well as one or two monlayer (ML) thick wetting layers are compared with calculations not using wetting layers.

3. Experiments and image analysis

Two 200 kV microscopes, a PHILIPS CM20 FEG and a HITACHI H-8110, have been used to investigate the QDs in the system CdSe/ZnSe. Plan-view diffraction contrast TEM images were taken to characterize the shape and size, and cross-sectional HREM images to reveal the atomic structure. The investigations were supported by energy-dispersive X-ray spectroscopy to gain chemical information of the wetting layer (see [12,13] for details and respective results).

The samples were grown by MBE on a (0 0 1) GaAs substrate with a 1 μm ZnSe buffer layer [21]. Three monolayers of CdSe were deposited at 230°C and then annealed at 310°C, the initial growth temperature of ZnSe. This corresponds to a thermal activation during the growth interruption after the deposition. The resulting QDs are capped by 85 nm of ZnSe. The plan-view samples were mechanically pre-thinned and subsequently dimpled to a thickness of 30 μm, and finally thinned by Xe^+ ion milling at 0.7 kV. The cross-sectional samples were prepared by face-to-face gluing, drilling of the cylinders out of the stack with the layers lying on the cylinder axis, cutting them into thin slices, polishing both sides down to approximately 100 μm, and finally by dimpling and ion-milling.

Fig. 2 shows typical experimental contrast features for a comparison with theoretical results. Fig. 2a is a slightly tilted HREM image of a single CdSe QD in the ZnSe matrix at an acceleration voltage of 200 kV and in approximately [1 1 0] orientation where only one set of the lattice fringes is seen with good contrast. Fig. 2b and c show two enlarged [0 0 1] plan-view diffraction contrast TEM micrographs with excitations of the (2 2 0)- and (0 4 0)-beams, respectively, and slightly different sample thicknesses.

The image simulations were carried out using the EMS software [22] or the CERIUS package. The latter is restricted to a maximum of 99 subslices, which is insufficient for highly distorted larger supercells. The parameters correspond to the microscopes used: acceleration voltage $U = 200$ kV, spherical aberration $C_s = 1$ mm, absorption potential factor $q = 0.1$, defocus spread $\delta = 8$ nm, beam-semiconvergence $\alpha = 0.5$ mrad. The beam apertures were chosen $\beta = 16$ and 2.0–6.0 nm^{-1} for cross-sectional HREM and plan-view TEM (diffraction contrast bright-field) images, respectively. All diffraction contrast thickness series were calculated with a defocus value of $\Delta = 25$ nm lying between the Gauss and the Scherzer focus. The HREM defocus series started at $\Delta = -25$ nm in steps of 25 nm up to 150 nm. The thicknesses chosen are $t = 7.4$, 10.2, and 13.6 nm (respectively $t = 9$, 13, and 17 nm for the larger cell).

4. Results

Though the theoretical annealing behavior of the QDs depends on the box size, the heating and cooling rates, and the outer forces applied, it enables the characterization of the stability of the QDs. Fig. 3 shows two typical results: the annealing of $\{1\,1\,2\}$ and $\{1\,1\,3\}$ QDs with 2 ML wetting layer is simulated for a heating rate of 24 K/ps (6 K/1000 steps). The potential energies are presented as a function of the simulation time. Selected regions of the QDs are shown in the insets characterizing the structure of the dots for the time step indicated by the arrows in the energy curves. While the

Fig. 1. Structures of different pyramidal quantum dot configurations: embedded and isolated spheres; $\{0\,1\,1\}$, $\{1\,1\,2\}$, $\{1\,1\,3\}$ and $\{1\,3\,6\}$ pyramids (ball and stick presentations, besides for $\{1\,1\,3\}$ where only the Cd atoms are shown as balls).

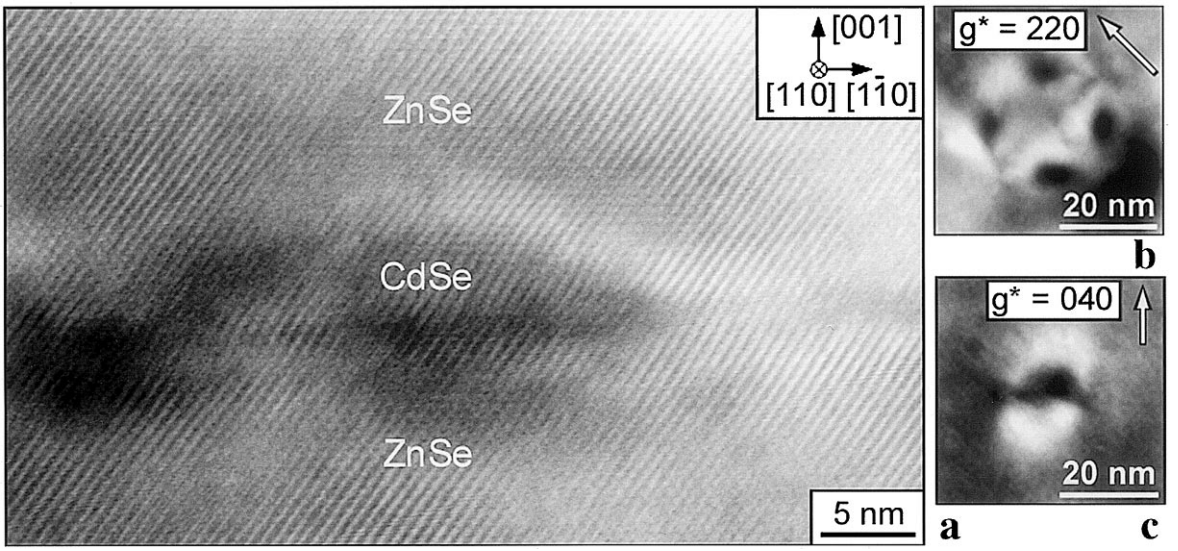

Fig. 2. Experimental ⟨1 1 0⟩ HREM image (a) and ⟨1 0 0⟩ plan-view diffraction contrast micrographs of CdSe QDs in ZnSe at 200 kV: bright field at (2 2 0) excitation (b) and dark field at (0 4 0) excitation (c).

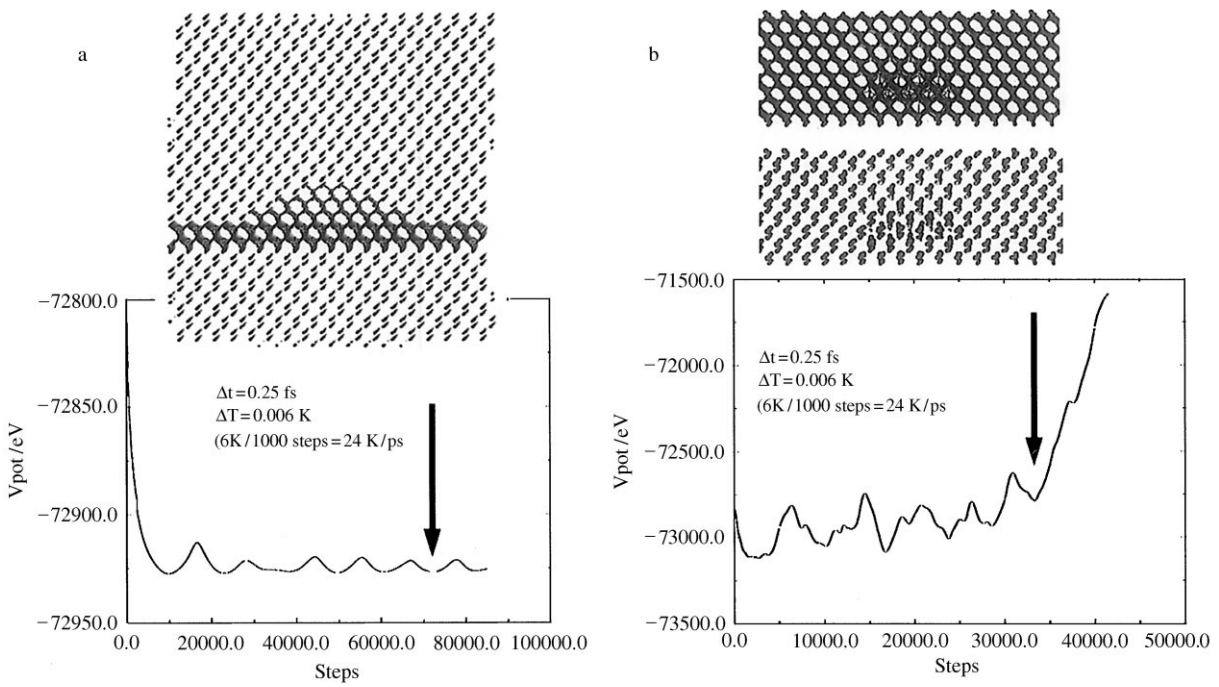

Fig. 3. Energy relaxation of a {1 1 3} (a) and a {1 1 2} (b) quantum dot (potential energy versus time steps, inset: perspective view of the structures for the step indicated by the arrows).

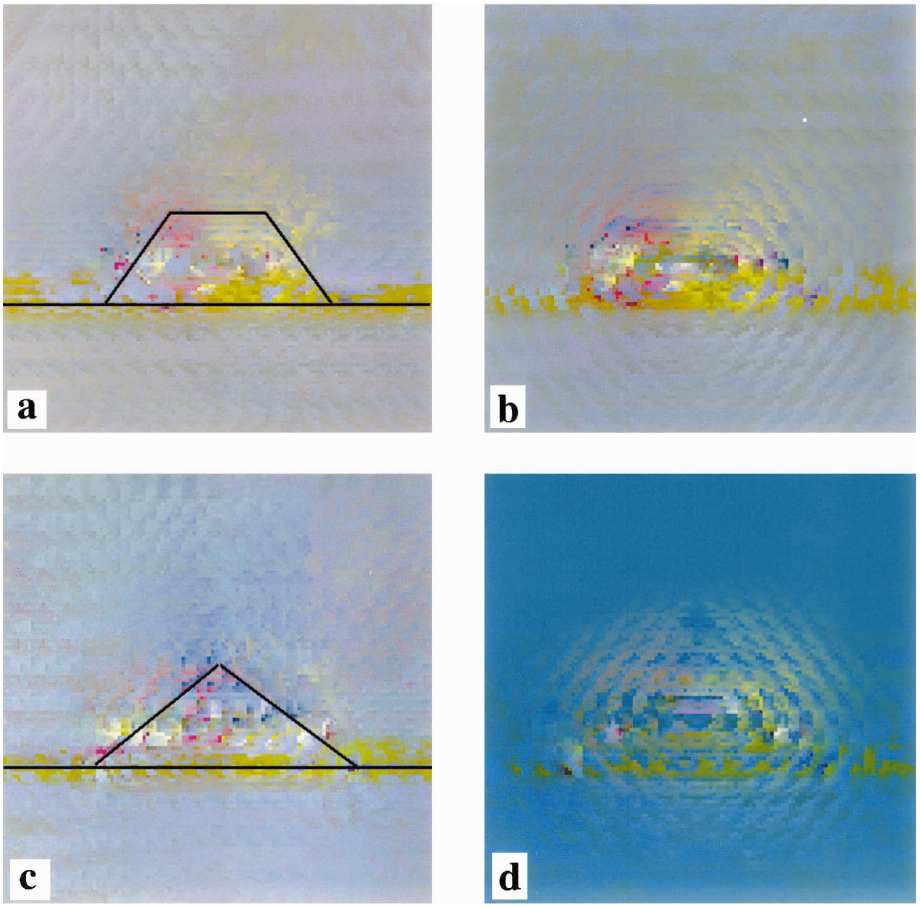

Fig. 4. Strain fields of the {0 1 1} (a, b) and the {1 1 3} (c, d) quantum dots at 600 K (a, c) and near 0 K (b, d) in $z = [1\,0\,0]$-projection ($x = [0\,1\,0]$, $y = [0\,0\,1]$, red: σ_{zz}, green: σ_{xz}, blue: σ_{yz})

{1 1 2} pyramid in Fig. 3b is amorphized after about 15 ps at 360 K, the {1 1 3} pyramid remains stable (cf. Fig. 3a). Comparing different simulations, however, similar to those shown in Fig. 3 but with larger boxes or smaller QDs, as well as using different facets yields analogous results: The flat QDs are more stable than the QDs with facets of a steeper descent. Larger boxes avoid the self-influencing effects and lead to a higher stability. However, because the direct Cd–Zn interaction is avoided in the potential, only the structural changes of the stable QDs have a well-defined physical meaning. Thus solely the stable QDs are used to evaluate the strain fields and to simulate the TEM and HREM images. The detailed analysis of the energetic behavior will be investigated in a forthcoming paper.

The resulting strain fields are presented in Fig. 4 as color-coded maps. Here, the strength of the normal strain component σ_{zz} is described by the intensity of red, whereas blue and green characterize the shear components σ_{xz} and σ_{yz}, resp., for the selected projection plane denoted by x, y, and z. In Fig. 4 the projection $z = (1\,0\,0)$ is chosen, i.e. x and y of the maps correspond to $(0\,1\,0)$ and $(0\,0\,1)$, respectively. The strains are evaluated by analyzing the atomic displacements during the relaxation of QDs. The characteristic strain fields are generated due to the lattice mismatch of about 7% in the present system. In Figs. 4a and b the strain fields of

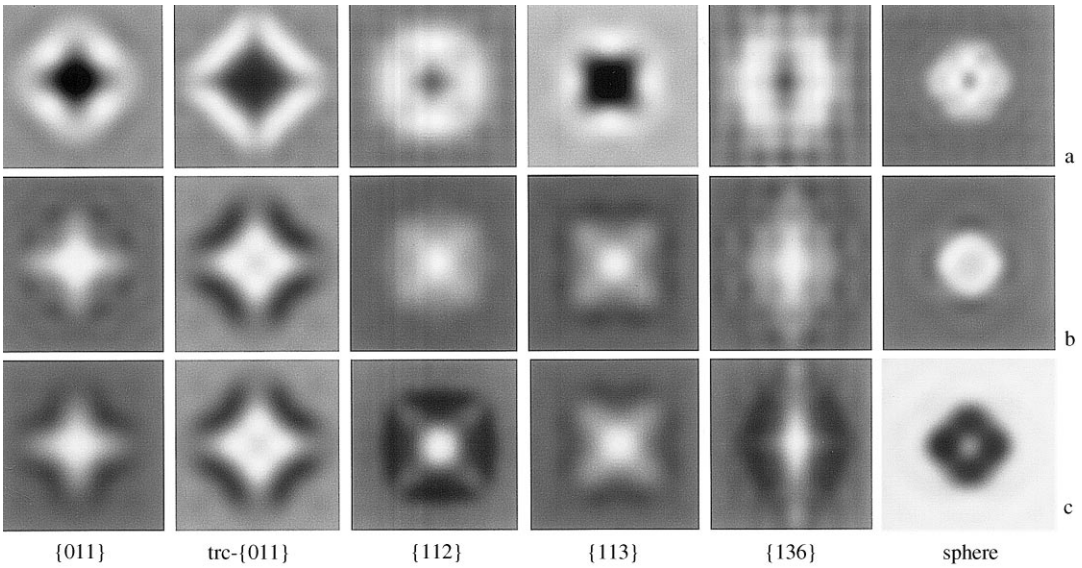

Fig. 5. Simulated bright-field (BF, apertures: 2 and 4 nm^{-1}, image axes parallel [1 1 0] with 7.4 nm length) diffraction contrast TEM images of QDs with different pyramidal shapes and sample thickness of $t = 7.4$ nm(a), 10.2 nm (b), 13.6 nm (c).

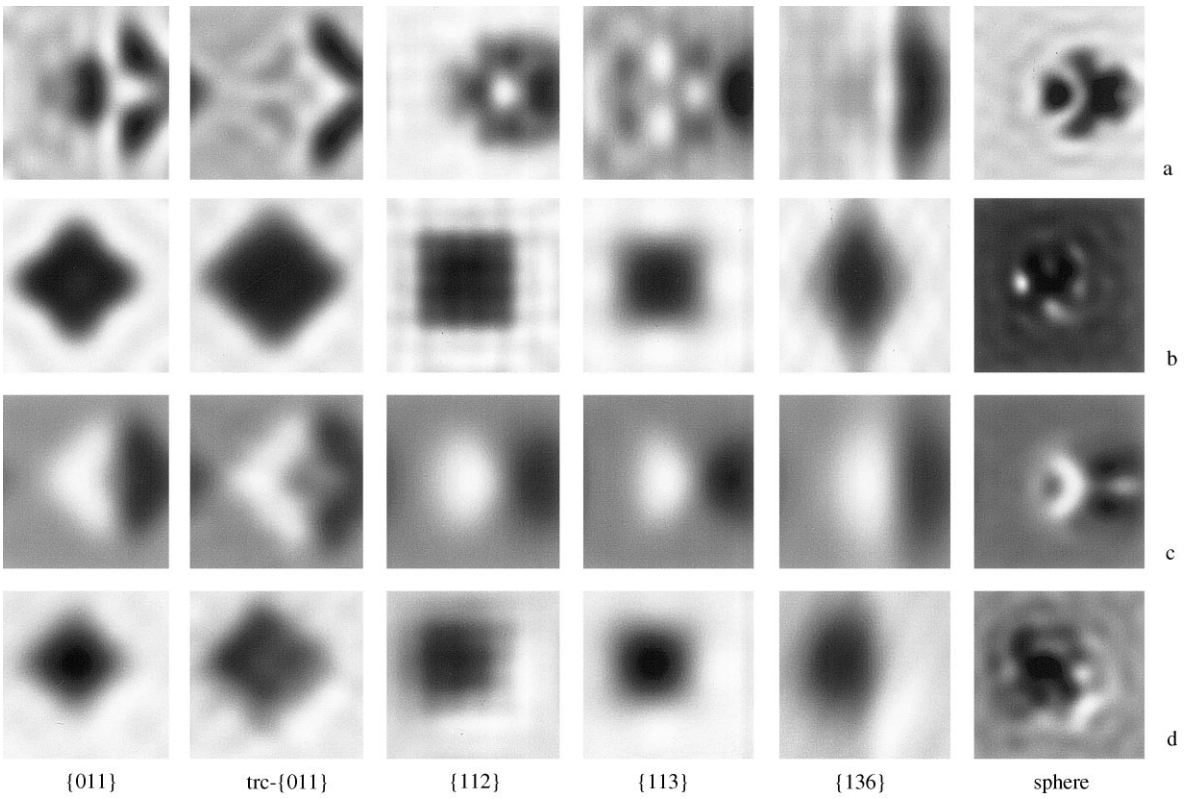

Fig. 6. Simulated dark-field (2 0 0 DF (a,c) and 2 2 0 DF (b,d), image axes parallel [1 1 0] with 7.4 nm length) diffraction contrast TEM images of QDs with different pyramidal shapes and sample thickness of $t = 7.4$ nm (a,b) and 13.6 nm (c,d).

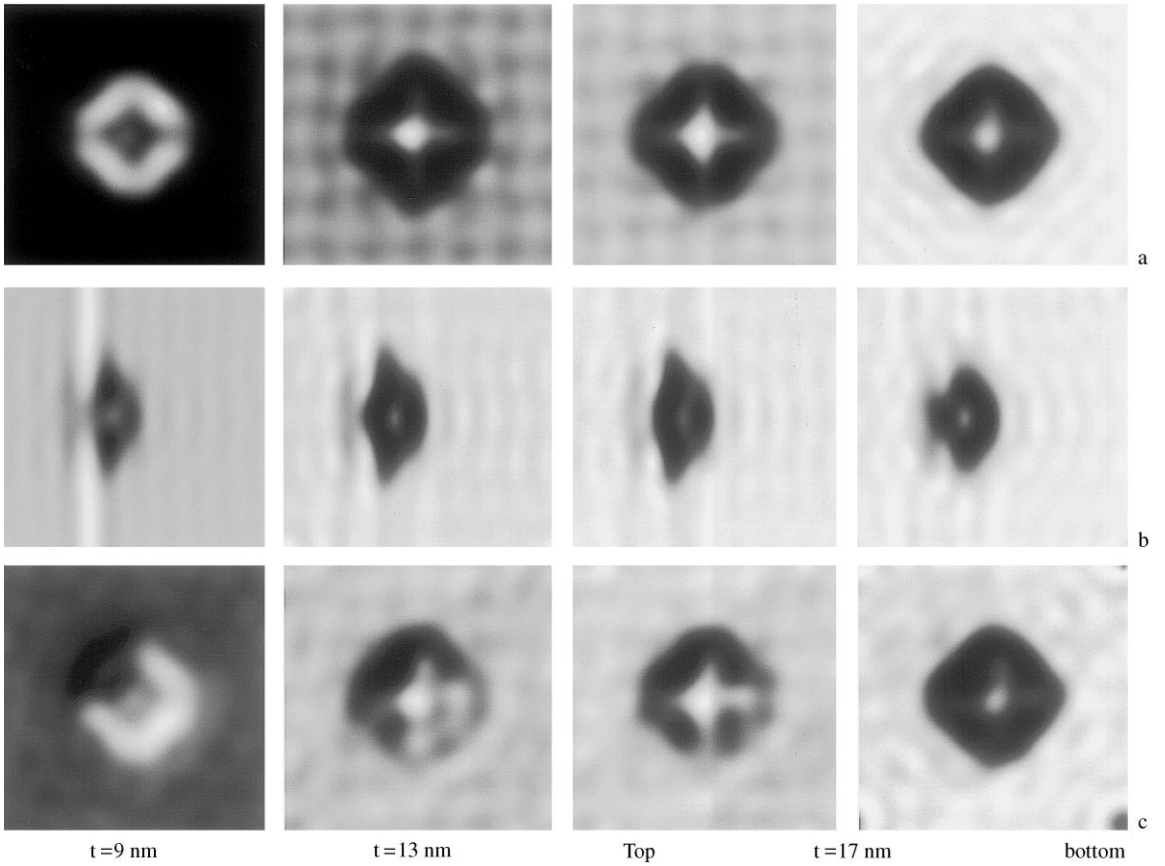

Fig. 7. Thickness series (t in nm, image axes parallel [1 1 0] with 9 nm length) of the {0 1 1} quantum dot within the larger box: symmetric [0 0 1] bright field (a), cross-sectional [1 1 0] bright field (b) and [0 0 1] tilted dark field with (2 2 0) excitation; depth position of the QD: 7 nm (left three columns) and 14 nm (right column).

a truncated {0 1 1} QD are shown in a snapshot at 600 K and in relaxed equilibrium, respectively, whereas in Figs. 4c and d the strain fields of the {1 1 3} dot are presented. The strain distribution can be compared with finite element calculations (FEM) of the elastic energy density of QDs, which, e.g., in [11] were performed for a 15 nm × 15 nm × 3 nm ZnSe substrate with a 0.5 nm CdSe wetting layer and a {0 1 1} facetted CdSe pyramid of 5 nm in base length along ⟨1 0 0⟩ directions. Furthermore, comparing the strain maps enables the direct understanding of the contrast features in TEM and HREM. The strain fields are almost symmetric for the relaxed structures, demonstrating the driving forces for the relaxation during annealing.

Fig. 5 shows the simulated zone-axis bright-field contrast of QDs with different facets (cf. Fig. 1 for the shapes): {0 1 1}, truncated {0 1 1}, {1 1 2}, {1 1 3}, {1 3 6}, and a sphere, resp. Three different thicknesses were chosen: $t = 7.4$ nm in (a), 10.2 nm (b), and 13.6 nm (c), to demonstrate the contrast reversal with increasing thickness. The simulations reveal that there are imaging conditions that allow a clear distinction of the different QDs by their characteristic contrast features due to the strain fields. Without strains solely a weak structure factor contrast arises. The pyramidal QDs with a steeper descent of the facets show a fourfold symmetry of their contrast features, however, this is clearly visible only at a symmetric bright-field incidence. The striations superimposed show that here

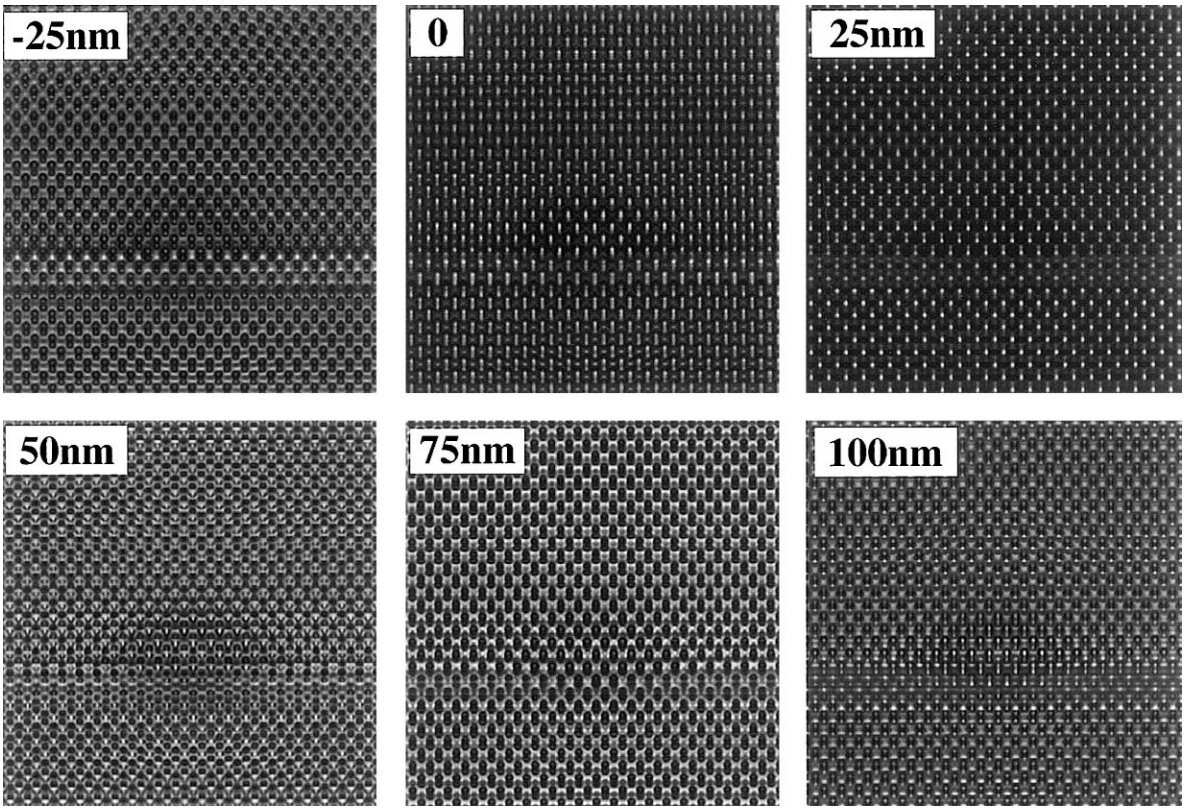

Fig. 8. Simulated [1 1 0] HREM defocus series (defocus Δ in nm, thickness $t = 7$ nm) of the truncated $\{0\,1\,1\}$ quantum dot.

some of the structures are not yet completely relaxed, their contrast depends sensitively on the objective aperture chosen in the simulations ($\beta = 2$–$4\ \mathrm{nm}^{-1}$). Especially at interfaces this results in some residual lattice fringe bending and in disturbances of the simulated images for larger thicknesses.

The comparison of the simulations with characteristic plan-view TEM images of CdSe/ZnSe QDs (see, e.g., Fig. 2, and [13]) allows one to conclude that most probably the observed pyramids have $\{0\,1\,1\}$ facets and base edges along $\langle 1\,0\,0\rangle$. Of all the different simulated contrast features only those as, e.g. Fig. 5c for the $\{0\,1\,1\}$-QD type match the black–white distribution of the experiment, because the sample thickness in the experiment is larger than 20 nm. Thus the observed contrast reversal leads to the assumption of truncated $\{0\,1\,1\}$-pyramids. The remaining discrepancy along the ledges of the pyramid may be due to some additional facetting, which has to be investigated in more detail later on. The orientation relationship of the CdSe QDs differs from that of InAs/GaAs in [5], probably due to the higher ionicity in II–VI semiconductors than in the III–V systems.

For comparison, Fig. 6 shows simulated dark-field diffraction contrast images of the same pyramids as in Fig. 5 using a (2 0 0) reflex (a,c) and a (2 2 0) one (b,d), as well as two different thicknesses $t = 7.4$ nm (a,b) and 10.6 nm (c,d). Dark-field images and/or tilted samples reveal the black-white contrast features with the well-known line of no contrast. In addition, Fig. 7 discusses various contrast-influencing factors using the example of the $\{1\,1\,3\}$ quantum dot, here, however, embedded in a larger supercell to understand the contrast scaling behavior. Thickness series of the plan-view and the cross-sectional orientation are presented in Fig. 7a,

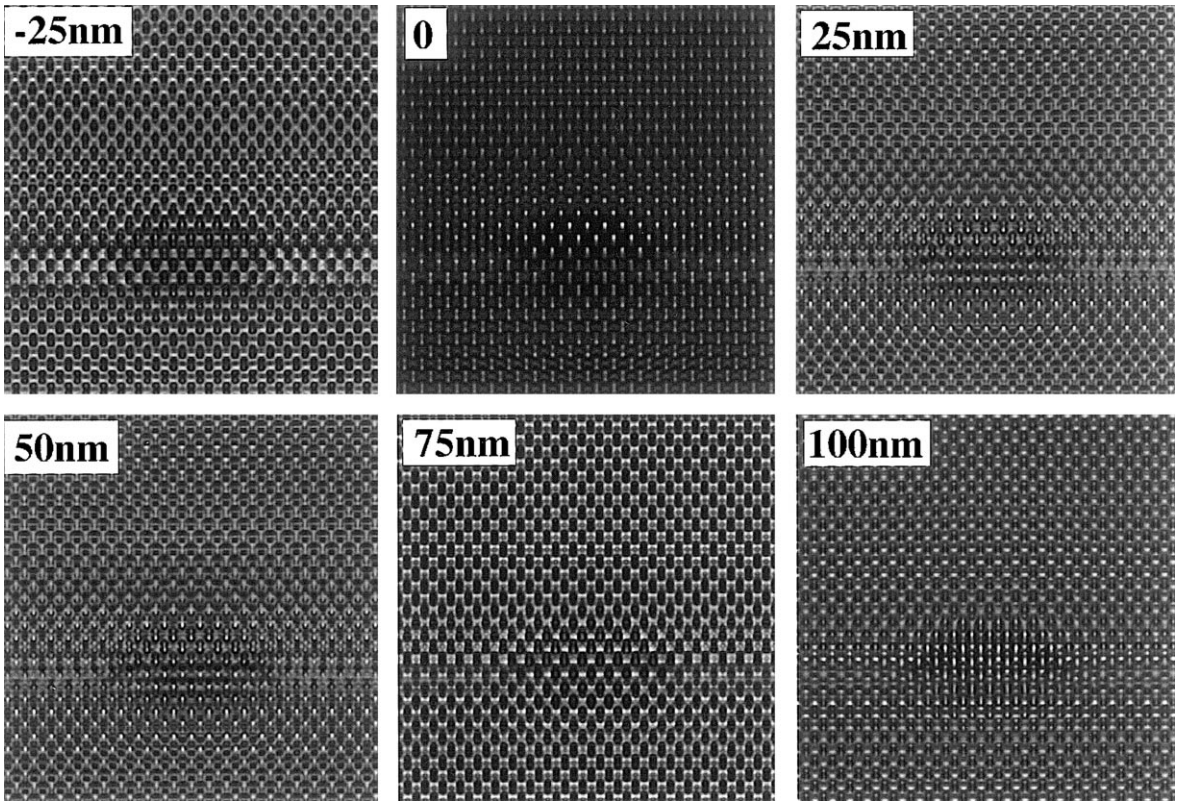

Fig. 9. Simulated [1 1 0] HREM defocus series (defocus Δ in nm, thickness $t = 9$ nm) of the complete $\{1\,1\,3\}$ quantum dot.

c and b, resp., for three different thicknesses $t = 9$, 13, and 17 nm. The contrast reversal between the thicknesses $t = 9$ and 13 nm is clearly evident. The cross-sectional TEM images of Fig. 7b reveal the existence of the wetting layers as dark or white stripes for smaller ($t = 9$ nm) and larger thicknesses ($t = 13$ nm) with respect to the background. The same strained QD in Fig. 7c is simulated for a tilted incident beam orientation. Exciting the (2 2 0) reflex approximately, the contrast no longer shows fourfold symmetry. Similarly, for dark fields, the contrast reversal of the black–white contrast lobes is coupled with the oscillation of the contrast according to different depths below the surface.

Finally, selected examples of various defocus series of HREM images of a truncated $\{0\,1\,1\}$ and a complete $\{1\,1\,3\}$ QD are shown in Figs. 8 and 9, respectively, to demonstrate the conditions of visualizing the atomic structures. The cross-sectional HREM images show a dumbbell-like contrast solely near the Scherzer focus, perhaps here the defocus spread of $\delta = 8$ nm and the divergence angle of $\alpha = 0.5$ mrad are still too optimistic for a comparison with the experiment. Nevertheless, the QDs are visible at certain defoci for the sample thicknesses of $t = 7$ and 9 nm considered. The pyramids mostly appear truncated. Striations of the HREM contrast of all atomic columns around the pyramid occur, the curvature of which is due to the strain field. The real shape of the QDs seems to be best pronounced near Scherzer focus $\Delta = 50$ nm as well as for $\Delta = -25$ nm and above 100 nm.

5. Conclusions

Structure simulations of CdSe quantum dots in a ZnSe matrix are performed to test the stability of

different configurations and to understand the underlying strain fields at an atomic level. The resulting relaxed QD structures are used to calculate the electron microscope contrast features. For the simulated as well as the experimental micrographs, the typical bright-field images of QDs show a wide contrast variability due to variations in thickness and orientation of the samples. The fundamental features of the diffraction contrast (black–white lobes and oscillation behavior) are maintained. Both in plan-view and in cross-sectional images there are contrasts due to the strain fields around the QDs having symmetries influenced by the shape of the dots. Under optimum imaging conditions the estimation of the size and the shape as well as the atomic displacements due to the misfit can be correlated. In the HREM images the pyramids seem to be almost truncated, and the visibility of the QDs is strongly influenced by the defocus, too. For appropriate specimen thicknesses and choosing suitable defoci the images may be interpretable with respect to the real size and shape of the QDs superimposed by the strain fields due to the lattice mismatch.

Acknowledgements

The authors would like to thank Prof. F. Henneberger and Dr. M. Rabe for providing the QD structures. H.K., R.S., and W.N. acknowledge financial support by the Deutsche Forschungsgemeinschaft in the framework of the Sonderforschungsbereich 296.

References

[1] D. Bimberg, M. Grundmann, N.N. Ledentsov, Quantum Dot Heterostructures, Wiley, Chicester, 1998.
[2] L.W. Wang, A. Zunger, Pseudopotential theory of nanometer silicon quantum dots, in: P.V. Kamat, D. Meisel (Eds.), Semiconductor Nanoclusters — Physical, Chemical, and Catalytic Aspects, Elsevier, Amsterdam, 1997.
[3] M. Lentzen, D. Gerthsen, A. Förster, K. Urban, Appl. Phys. Lett. 60 (1992) 74.
[4] O. Stier, M. Grundmann, D. Bimberg, Phys. Rev. B 59 (1999) 5688.
[5] S. Rouvimov, K. Scheerschmidt, Phys. Status Solidi A 150 (1995) 471.
[6] X.Z. Liao et al., Phys. Rev. B 58 (1998) R4235.
[7] D. Lepski, Phys. Status Solidi A 66 (1980) 479.
[8] D. Lepski, Phys. Status Solidi A 23 (1974) 543.
[9] S. Christiansen, M. Albrecht, H.P. Strunk, H.J. Maier, Appl. Phys. Lett. 64 (1994) 3617.
[10] Y. Androussi, T. Benabbas, A. Levebvre, Philos. Mag. Lett. 79 (1999) 201.
[11] H. Kirmse, W. Neumann, T. Wiebach, R. Köhler, K. Scheerschmidt, D. Conrad, Mater. Sci. Eng. B 69 (2000) 361.
[12] H. Kirmse, R. Schneider, R. Rabe, W. Neumann, F. Henneberger, Appl. Phys. Lett. 72 (1998) 1329.
[13] H. Kirmse, R. Schneider, K. Scheerschmidt, D. Conrad, W. Neumann, J. Microsc. 194 (1999) 183.
[14] C.W. Gear, Numerical Initial Value Problems in Ordinary Differential Equations, Prentice-Hall, Englewood Cliffs, NJ, 1971.
[15] F.H. Stillinger, T.A. Weber, Phys. Rev. B 31 (1985) 5262.
[16] J. Tersoff, Phys. Rev. B 39 (1989) 5566.
[17] H. Balamane, T. Halicioglu, W.A. Tiller, Phys. Rev. B 46 (1992) 2250.
[18] Z.Q. Wang, D. Stroud, A.J. Markworth, Phys. Rev. B 40 (1989) 3129.
[19] D. Conrad, K. Scheerschmidt, U. Gösele, Appl. Phys. A 62 (1996) 7.
[20] CERIUS program package, Molecular Simulations Inc., San Diego.
[21] M. Rabe, M. Lowisch, F. Henneberger, J. Crystal. Growth 185 (1998) 248.
[22] P.A. Stadelmann, Ultramicroscopy 21 (1987) 131.